High power conditioning and benchmarking of planar nitrogen-incorporated ultrananocrystalline diamond field emission electron source

Jiahang Shao[1,*], Mitchell Schneider[2,‡], Gongxiaohui Chen[3,‡], Tanvi Nikhar[2],
Kiran Kumar Kovi[4], Linda Spentzouris[3], Eric Wisniewski[1], John Power[1],
Manoel Conde[1], Wanming Liu[1], and Sergey V. Baryshev[2,†]

[1]Argonne National Laboratory, Lemont, Illinois 60439, USA
[2]Michigan State University, East Lansing, Michigan 48824, USA
[3]Illinois Institute of Technology, Chicago, Illinois 60616, USA
[4]Euclid Techlabs LLC, Bolingbrook, Illinois 60440, USA

Planar nitrogen-incorporated ultrananocrystalline diamond [(N)UNCD] has emerged as a unique field emission source attractive for accelerator applications because of its capability to generate a high charge beam and handle moderate vacuum conditions. Most importantly, (N)UNCD sources are simple to produce: Conventional high aspect ratio isolated emitters are not required to be formed on the surface, and the actual emitter surface roughness is on the order of only 10–100 nm. A careful reliability assessment of (N)UNCD is required before it may find routine application in accelerator systems. In the present study using an L-band normal conducting single-cell rf gun, a (N)UNCD cathode has been conditioned to ~42 MV/m in a well-controlled manner. It reached a maximum output charge of 15 nC corresponding to an average current of 6 mA during an emission period of 2.5 μs. Imaging of the emission current revealed a large number of isolated emitters (density over $100/cm^2$) distributed on the cathode, which is consistent with previous tests in dc environments. The performance metrics, the emission imaging, and the systematic study of emission properties during rf conditioning in a wide gradient range assert (N)UNCD as an enabling electron source for rf injector designs serving industrial and scientific applications. These studies also improve the fundamental knowledge of the practical conditioning procedure via a better understanding of the emission mechanisms.

I. INTRODUCTION

The field emission cathode (FEC) is a viable choice for rf injectors in many industrial and scientific applications [1–10]. It has several clear advantages compared to thermionic cathodes and photocathodes. First, it is simple, as no heating system or laser is required to facilitate electron emission [6,7,9]. Second, it has the capability to deliver a high output current with maximum current densities on the order of 10^8 A/cm^2 [5]. Third, it has the potential to reach ultralow emittance and energy spread via various gating methods [4,6,11,12]. The way is being paved toward the realization of high-performance FEC-based injectors.

Maintaining high FEC performance over long-term operation remains an important goal. Various advanced field emitter materials and configurations are currently under intense investigation in dc and rf environments. For high power vacuum systems, materials of interest are often carbon-derived substances such as the carbon nanotube [9,13,14], nanocrystalline diamond (NCD) [15–17], nitrogen-incorporated ultrananocrystalline diamond [(N)UNCD] [6,8,18], and others [19–21]. For aggressive high oxygen content environments like thrusters, diamond and boron nitride are under intense study [22]. Configurations of interest include Spindt-type high aspect ratio single emitters or emitter arrays and planar nanometer-roughness emitters.

Planar (N)UNCD is a promising material that yields a high current and allows for simplicity and scalability in fabrication. Although the exact mechanism of field emission from diamond surfaces is still under debate, previous experiments have shown that emission originates from the sp^2 grain boundaries [23,24]. The high grain boundary density of (N)UNCD material could therefore potentially

lead to a high current density. To date, planar (N)UNCD cathodes have been tested and shown to perform in normal conducting rf guns (20–70 MV/m) [6,8], in a superconducting rf gun (1 MV at 2–4 K) [25], and in dc setups (1–20 MV/m) [18]. The full operational range, from turn-on up to the breakdown field, must be explored systematically before (N)UNCD can be considered for accelerator applications. These may include industrial systems (surface fields 1–20 MV/m) or scientific systems (surface fields up to 100 MV/m). Addressing the fundamental emission mechanism puzzle is also critical for successful (N)UNCD deployment.

The study presented here extends planar (N)UNCD cathode high pulsed power characterization during rf conditioning. Detailed emission properties were recorded as the macroscopic E field was conditioned from ∼8 to ∼42 MV/m; these included the current and current density, effective emission area A_e, field enhancement factor β and microscopic electric field, turn-on field, and temporal emission stability. The metrics evolution of the emission parameters was analyzed and interpreted in the framework of a unique density-of-states structure of (N)UNCD [26]. High-resolution imaging of the (N)UNCD emitting surface in the rf gun environment showed a large number of localized emitters (density over $100/cm^2$) distributed across the surface. This result is consistent with results obtained in dc setups [18,27,28].

This paper is organized as follows: Sec. II presents the cathode preparation; Sec. III introduces the experimental setup; Sec. IV provides a detailed description of the experimental methods, procedures, and results; Sec. V discusses the experimental results and presents a hypothesis for the emission evolution mechanism during rf conditioning; and Sec. VI summarizes the study and outlines future work.

II. CATHODE PREPARATION

A. Cathode assembly

The cathode plug (34.7 mm tall and 20 mm in diameter) is designed as a three-part assembly with an aluminum body, an aluminum middle piece, and a stainless steel top piece, as illustrated in Fig. 1. The design meets the installation requirements of the L-band photocathode rf gun test stand [8,12,29,30] and enables convenient material synthesis onto the thin top part. The parts are aligned with each other and assembled together using internal vented screws. The electrical contact between the cathode assembly and the rf gun is ensured by a spring around the cathode body.

B. Cathode synthesis

The synthesis procedure of depositing the (N)UNCD material onto the top piece is described as follows. (i) The top piece was polished to 100-nm-level roughness to avoid any high aspect ratio site-induced emission. The stylus profilometer measurement and the spatial Fourier
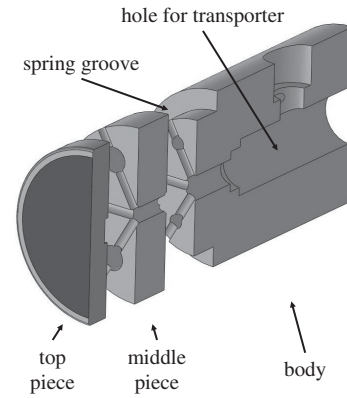

FIG. 1. Cutaway drawing of the cathode assembly. The dark part of the top piece represents the (N)UNCD material. The vented screws holding the parts together are not shown.

analysis [31,32] suggest the maximum physical field enhancement factor is lower than 1.01, as illustrated in Fig. 2. (ii) A molybdenum buffer layer of 150 nm thickness was deposited using magnetron sputtering. (iii) The top piece underwent an ultrasonic seeding procedure that made use of diamond slurry (Adamas Technologies) with a particle size of 5–10 nm. (iv) The (N)UNCD material was deposited
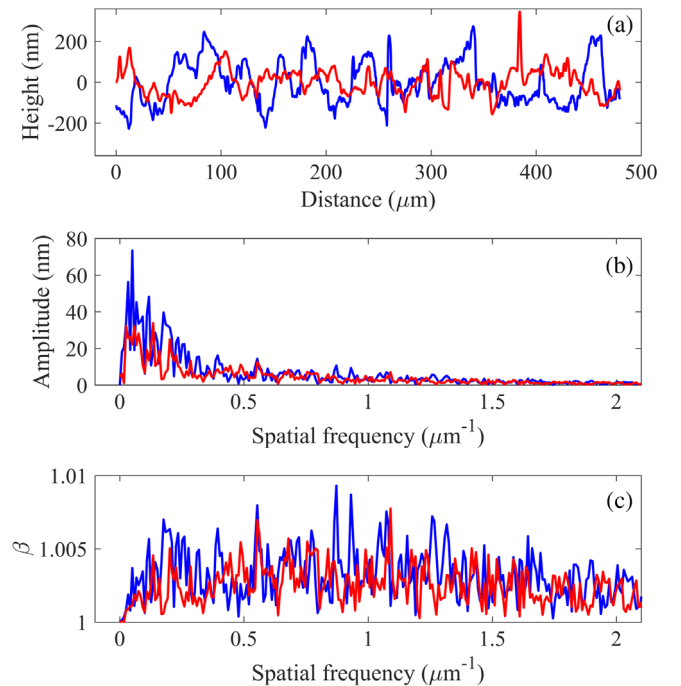

FIG. 2. Surface roughness analysis of the polished top piece before (blue lines) and after (red lines) the high power test. The two measurements were conducted at two close sites within 1 mm distance. (a) Surface profile. Before the high power test, the peak-to-peak and root-mean-square roughness is 503 and 108 nm, respectively. After the high power test, the peak-to-peak and root-mean-square roughness is 503 and 66 nm, respectively. (b) Spatial frequency spectrum. (c) Field enhancement factor.
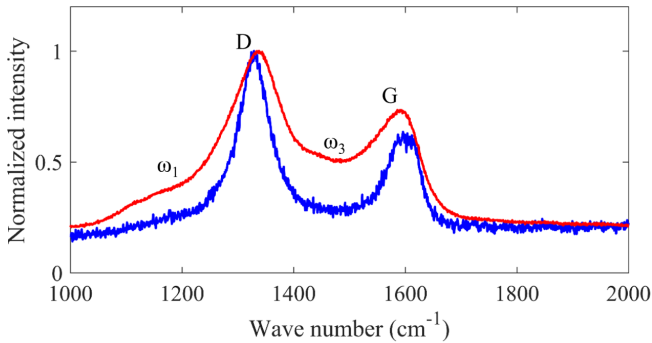
FIG. 3. Raman spectra taken at different locations across the (N)UNCD surface showing carbon phase variation. Measurements were performed using a primary probe wavelength of 633 nm. Red curve: Location with nearly canonical (N)UNCD spectra containing D and G bands intrinsic to UNCD and ω_1 and ω_3 bands showing the presence of hydrocarbon transpolyacetylene chains in grain boundaries. Blue curve: Location demonstrating stronger graphitization of UNCD in which the right-hand shift of the G band suggests that grain boundaries are better crystallized due to a higher local synthesis temperature signified by the absence of ω_1 and ω_3 bands of t-PA that decomposes above 1100 K.

using microwave-assisted plasma chemical vapor deposition (Lambda Technologies Inc.) operated at 915 MHz. During growth, the total pressure was 56 Torr, the microwave power was 2.3 kW, and individual gas flows for Ar, CH_4, and N_2 were 3, 160, and 40 sccm, respectively.

During the growth of (N)UNCD via chemical vapor deposition, there are competing processes that form the diamond sp^3 phase and the graphitic sp^2 phase. These should be in the right proportion to allow mechanical strength and adhesion and to obtain high conductivity and emission efficiency. Here, high emission efficiency means a low turn-on field (1–10 MV/m) and a high field enhancement factor (100–1000). Given that grain boundaries (sp^2 phase) facilitate emission, the (N)UNCD efficiency can be tuned through the sp^3-to-sp^2 ratio [16,33]. Compared to our previous growth protocol executed at 850°C [8], the synthesis temperature was increased by 50°C to induce a larger fraction of ordered graphitic sp^2 phase [16].

Raman spectroscopy revealed that the graphitic phase increased (as compared to Ref. [8]) but at the same time appeared to nonuniformly distribute across the surface, as illustrated in Fig. 3. Some locations (red curve) demonstrated nearly canonical (N)UNCD spectra. Meanwhile, other locations (blue curve) showed stronger graphitization due to a higher local temperature which is evidenced by the disappearance of ω_1 and ω_3 bands associated with transpolyacetylene (t-PA) [34]. All characterized locations demonstrate the strong D band representing the diamond grain sp^3 host matrix and the G band that is associated with the graphitic sp^2 grain boundaries. Locations such as that represented by the blue curve in Fig. 3 are expected to have

grain boundaries that are better crystallized compared to locations such as that represented by the red curve.

In spray-deposited films comprised of diamond and graphite powders mixed at varied diamond-to-graphite ratios, that are model systems with predesigned nonuniform diamond-to-graphite distribution, electron emission was found to be nonuniform across the surface [27]. Therefore, it could be speculated that such a nonuniform diamond-to-graphite (sp^3-to-sp^2) content distribution is responsible for the nonuniform emission across the nanodiamond surface. This was also observed in previous dc studies [18,28], and in both cases it was shown that surface topography cannot explain the enhanced field emission at a low turn-on field.

The average work function of the (N)UNCD surface after deposition was measured to be 4.0 eV by a Kelvin probe, close to the ones reported in previous studies [35,36].

III. EXPERIMENTAL SETUP

The experiment was conducted using the Argonne Cathode Test-stand (ACT) beam line at the Argonne Wakefield Accelerator (AWA) facility [8,12,29,30], which is illustrated in Fig. 4. The ACT beam line is equipped with a single-cell normal conducting photocathode rf gun operated in the L band at 1.3 GHz. The beam line currently runs at a 2 Hz repetition rate with a full width half maximum (FWHM) pulse length of 6 μs. Cathodes with various shapes and materials can be tested thanks to the detachable cathode design. A frequency tuner also allows the cathodes to be tested at a wide range of longitudinal positions inside the cavity, which results in a drastically different field on the cathode surface for the same input rf power [29]. In this experiment, the cathode surface was set to be flush with the rf gun back wall. At this position, ~227 W of input power is required to obtain a 1 MV/m cathode electric field. Vacuum in the beam line was maintained below 5×10^{-9} Torr.

Diagnostics used in the experiment include a directional coupler to monitor the input and reflected rf power, an rf pickup installed at the gun side wall to detect the field profile, an aluminum block acting as a Faraday cup at the gun exit to collect the field emission current, and yttrium-aluminum-garnet (YAG) screens to observe the beam transverse profile along the beam line. There was also an imaging
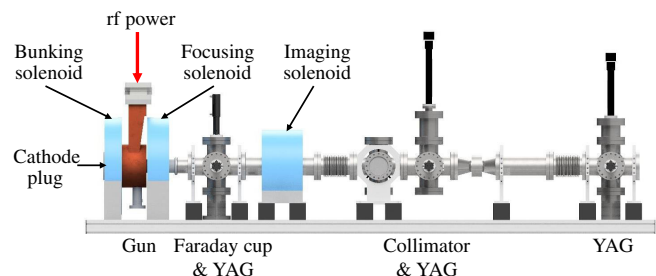

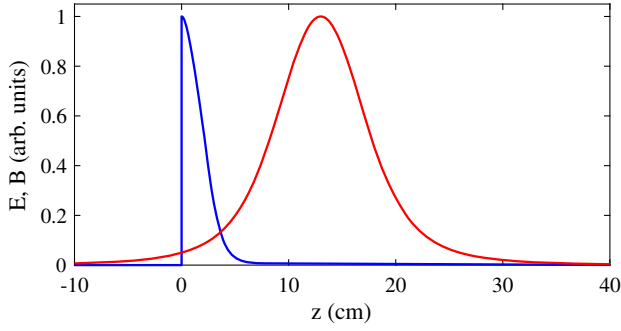FIG. 4. Layout of the ACT beam line at AWA.

FIG. 5. Longitudinal field profile of the normalized electric field of the rf gun (blue curve) and the normalized magnetic field of the focusing solenoid (red curve). The electric field decreases monotonically from the cathode ($z = 0$) to the gun exit ($z = 7.7$ cm) due to the single-cell design.

system consisting of solenoids and a collimator to obtain the field emitter distribution with a high resolution [12,30]. A photomultiplier tube with a fluorescent screen sensitive to x rays was placed near the gun for machine interlock purposes in the event of rf breakdown [37]. The strength of the focusing solenoid (denoted as B_f) was used to maximize the electron beam capture ratio at the Faraday cup. The longitudinal on-axis field profiles of the rf gun and the focusing solenoid are illustrated in Fig. 5.

IV. HIGH POWER TEST

A. Field emission charge collection

The capture ratio of the Faraday cup depends on the rf gun field as well as the focusing solenoid strength. Determining the capture ratio under various circumstances is critical for the interpretation of the field emission properties in the measurement. This subsection introduces the simulation and experimental efforts to ensure effective charge collection as well as to determine the capture ratio.

In this subsection, $|E_c(t)|$ denotes the macroscopic cathode field amplitude within the 6 μs rf pulse, $E_{c,\max}$ denotes its maximum value, and $E_c(t) = |E_c(t)|\cos(\omega t)$ denotes the transient cathode field where ω is the operation frequency. Since the rf pulse length is much longer than the rf cycle ($1/1.3$ GHz = 769.2 ps), the slow variation of the field amplitude is ignored and $|E_c(t)|$ is treated as a constant $|E_c|$ in each rf cycle. η_{cycle} and η_{pulse} denote the capture ratio within one rf cycle and one rf pulse, respectively.

In the equations that follow, the units of the electric field, emission current, effective emission area, and work function are V/m, A, m^2, and eV, respectively.

1. Capture ratio within one rf cycle

According to the Fowler-Nordheim (F-N) equation, the transient field emission current when the cathode field is positive [$\cos(\omega t) > 0$] can be expressed as [37,38]
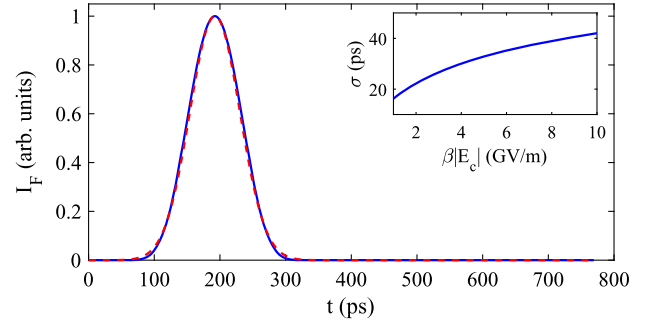

FIG. 6. Emission profile within one rf cycle based on Eq. (1) (blue solid line) and its Gaussian distribution approximation (red dashed line). Inset: The standard deviation of the Gaussian distribution as a function the maximum microscopic cathode field.

$$I_F(t) = \frac{1.54 \times 10^{-6} \times 10^{4.52\phi^{-0.5}} A_e [\beta E_c(t)]^2}{\phi}$$
$$\times \exp\left[-\frac{6.53 \times 10^9 \phi^{1.5}}{\beta E_c(t)}\right], \tag{1}$$

where ϕ is the work function. The emission profile can be approximated by a Gaussian distribution [39] whose standard deviation σ depends on the maximum microscopic cathode field $\beta|E_c|$, as illustrated in Fig. 6.

As the emission period covers 180° in the rf cycle, electrons experience different accelerating fields and focusing strengths depending on their emitting phases. A portion of the field emission electrons cannot be captured by the Faraday cup due to the finite gun aperture (40 mm in diameter) and the limited Faraday cup size (64 mm tall and 71 mm wide), as well as the beam dynamics inside the rf gun.

Beam dynamics simulations with ASTRA [40] have therefore been conducted to examine the capture ratio, in which the electrons were emitted uniformly from the (N)UNCD covered area (18 mm in diameter) on the cathode with an initial kinetic energy of 0.1 eV. The longitudinal emission profile was set to be Gaussian with σ determined by the fitted $\beta|E_c|$ (introduced in the following sections). The blue line in Fig. 7 illustrates an example of the simulated capture ratio η_{cycle} dependence on focusing solenoid strength B_f, with $|E_c|$ of 42 MV/m, β of 179, and $\beta|E_c|$ of 7.5 GV/m. It shows that over 90% of the emitted electrons can be captured by the Faraday cup when B_f is set to 750 G.

2. Capture ratio within one rf pulse with fixed $E_{c,\max}$

Within the 6 μs rf pulse, the macroscopic cathode electric field amplitude varies due to the finite pulse length and the filling time of the standing-wave cavity, as illustrated in Fig. 8. Therefore, η_{cycle} is also time dependent, and η_{pulse} can be defined as
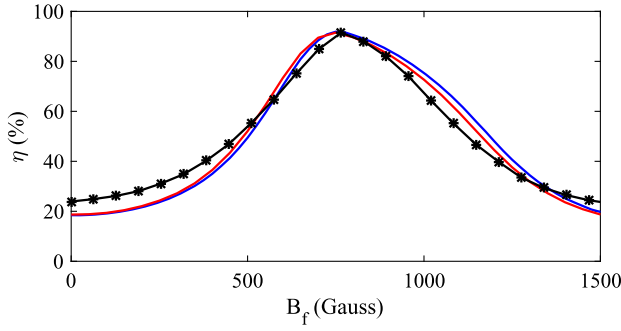
FIG. 7. The capture ratio of the Faraday cup with β of 179. Blue line: η_{cycle} with $|E_c|$ of 42 MV/m; red line: η_{pulse} with $E_{c,\text{max}}$ of 42 MV/m; black line: measured charge at $E_{c,\text{max}}$ of 42 MV/m with the maximum value normalized to the highest capture ratio in the simulation.
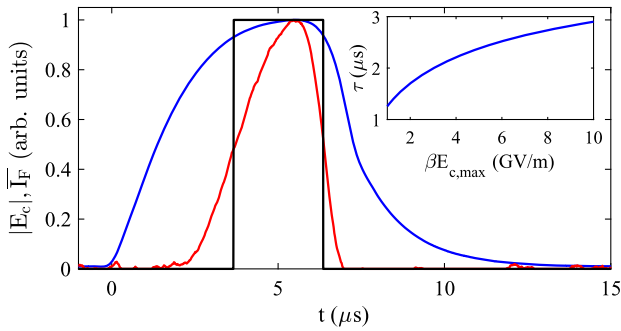

FIG. 8. Blue line: The normalized cathode field amplitude $|E_c(t)|$ measured by the rf pickup. Red line: The predicted average emission current $\overline{I_F(t)}$ by Eq. (3). Black line: The square pulse approximation of the emission profile. Inset: The width of the square emission profile as a function of $\beta E_{c,\text{max}}$.

$$\eta_{\text{pulse}} = \frac{\int \eta_{\text{cycle}}(t)\overline{I_F(t)}dt}{\int \overline{I_F(t)}dt}, \tag{2}$$

where $\overline{I_F(t)}$ denotes the average emission current within one rf cycle that can be expressed as [37]

$$\overline{I_F(t)} = \frac{5.7 \times 10^{-12} \times 10^{4.52\phi^{-0.5}} A_e [\beta|E_c(t)|]^{2.5}}{\phi^{1.75}}$$

$$\times \exp\left[-\frac{6.53 \times 10^9 \phi^{1.5}}{\beta|E_c(t)|}\right]. \tag{3}$$

In ASTRA simulations of the capture ratio within one rf pulse with fixed $E_{c,\text{max}}$, η_{cycle} at various field levels were individually studied in the same manner as described in the previous subsection; then η_{pulse} was calculated using the predicted emission profile as illustrated in Fig. 8. For each $|E_c|$, β was assumed to be constant and σ of the longitudinal emission profile was adjusted based on $\beta|E_c|$. The red line in Fig. 7 illustrates the η_{pulse} dependence on focusing

solenoid strength B_f, with $E_{c,\text{max}}$ of 42 MV/m and β of 179, which shows good agreement with the experimental results.

In Fig. 7, the blue and the red lines are very similar to each other, which implies that η_{pulse} is dominated by η_{cycle} at $E_{c,\text{max}}$. This can be understood since $\overline{I_F(t)}$ is highly sensitive to $|E_c|$. As illustrated in Fig. 8, $\overline{I_F(t)}$ drops to 1% of its maximum value when $|E_c|$ decreases by only 20%. The capture ratio study can therefore be simplified by using a square emission profile with an average emission current of $\overline{I_{F,\text{max}}}$ calculated by using $|E_c| = E_{c,\text{max}}$ in Eq. (3), as illustrated in Fig. 8. The width of the square pulse is set as $\tau = \int \overline{I_F(t)}dt/\overline{I_{F,\text{max}}}$ so as to keep the same charge. It depends on $\beta E_{c,\text{max}}$, as calculated by Eq. (3) and illustrated in the inset in Fig. 8.

3. Capture ratio within one rf pulse with various $E_{c,\text{max}}$

The dependence of $\overline{I_{F,\text{max}}}$ on $E_{c,\text{max}}$ can be plotted in the $1/E_{c,\text{max}}$-$\lg(\overline{I_{F,\text{max}}}/E_{c,\text{max}}^{2.5})$ coordinate (also known as the F-N coordinate). When space-charge effects do not significantly influence field emission, the dependence of $\lg(\overline{I_{F,\text{max}}}/E_{c,\text{max}}^{2.5})$ on $1/E_{c,\text{max}}$ is linear [41,42], and then β and A_e can be found from a fit as follows [37]:

$$\beta = \frac{-2.84 \times 10^9 \phi^{1.5}}{s},$$

$$A_e = \frac{10^{y_0}\phi^{1.75}}{5.7 \times 10^{-12} \times 10^{4.52\phi^{-0.5}}\beta}, \tag{4}$$

where s and y_0 are the slope and the y axis intercept of the linear dependence, respectively.

Experimental studies of emission properties usually record various electric field levels and the corresponding field emission current in order to fit β and A_e. The capture ratio under these field levels may not be the same, especially in rf structures with complicated geometries, which could lead to inaccurate results. This effect, however, was seldom considered in previous research.

This effect has been carefully simulated in the presented study. As described previously, the emission profile in this simulation step was approximated by a square pulse with its width determined by $\beta E_{c,\text{max}}$. The value of β paired with each $E_{c,\text{max}}$ was kept constant with the assumption that the surface condition does not change during the measurement. This assumption is valid, since measurements usually took less than 300 rf pulses (2.5 min) without any rf breakdown, compared to the entire experimental period of tens of hours with thousands of rf breakdowns. The variation of $E_{c,\text{max}}$ in the simulation was set to be 20%, close to the one used in the experiment, which was limited by the minimal detectable charge of the Faraday cup. The simulation results, as illustrated in Fig. 9, suggest that a similar capture ratio (with a maximum difference of less than 2%) can be achieved
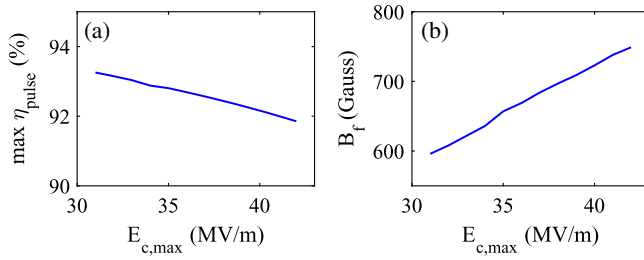
FIG. 9.   The maximum η_{pulse} (a) and the corresponding B_f (b) as a function of $E_{c,\text{max}}$. In this simulation, β is fixed at 179.

by adjusting B_f, which supports the accuracy of the fitted results in the following sections.

B. Field emitter distribution

The field emitter distribution on the (N)UNCD cathode was studied with a low resolution by taking regular YAG images at the gun exit and with a high resolution using the *in situ* field emission imaging system at the downstream end of the beam line.

1. Low-resolution observation at the gun exit

Because of the detachable cathode design, field emission electrons may come from the edge of the cathode or insertion hole rather than the cathode itself. The two sources cannot be distinguished by the Faraday cup. Therefore, a YAG screen (denoted as YAG$_1$) located at the same location as the Faraday cup was used to evaluate the emission current from these sources.

ASTRA simulations have been conducted to predict the transverse electron distribution at the YAG$_1$ position. Six $\varnothing 0.2$ mm field emitters were placed on the cathode edge in the simulation, as illustrated in Fig. 10(a). Electrons emit uniformly within each emitter with an initial kinetic energy of 0.1 eV. They emit during 180° of the rf phase when the electric field is positive. The longitudinal profile during one rf cycle has a Gaussian distribution as described in previous sections. The simulated YAG$_1$ image is illustrated in Fig. 10(b). The line-shaped pattern is caused by the wide energy spread of the beam from the broad emission phase, which is common for field emission in rf guns [12,43–46].

The simulation results are compared with the experimental observation under the same $E_{c,\text{max}}$ and B_f to identify the source of emission current. With the (N)UNCD cathode, the line-shaped pattern marked by the red circle in Fig. 10(c) has a similar shape and location as that caused by an edge emitter in the ASTRA simulation, which indicates that there was one emitter at the edge of the cathode or insertion hole. The rest of the observed pattern on YAG$_1$ is caused by emitters on the (N)UNCD material, whose total brightness is much higher than that of the edge emitter. Therefore, the collected charge should be dominated by (N)UNCD emitters rather than the edge emitter. In comparison, the experimental
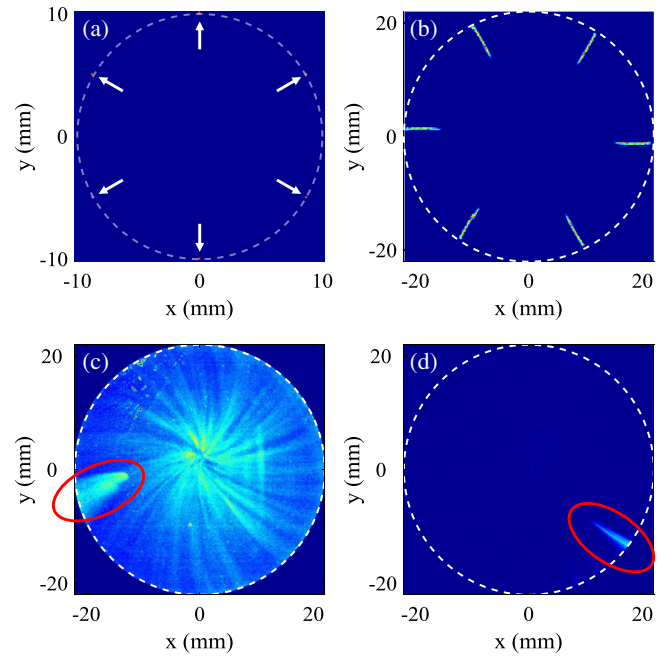

FIG. 10.   (a) The initial edge emitters distribution used in the ASTRA simulation. The white dashed circle represents the $\varnothing 20$ mm cathode edge, and the white arrows point to the six emitters. (b) Simulated transverse distribution of field emission electrons from the six emitters on YAG$_1$. (c) Experimental observation with the (N)UNCD cathode on YAG$_1$. (d) Experimental observation with a molybdenum cathode on YAG$_1$. In (b)–(d), the images were simulated or taken with the same $E_{c,\text{max}}$ and B_f settings. The white dashed circle represents the $\varnothing 44$ mm YAG boundary. The red circles mark electrons from edge emitters.

result using a molybdenum cathode without (N)UNCD material clearly shows that the emission was mainly from edge emitters, as illustrated in Fig. 10(d).

2. High-resolution observation at downstream end of the beam line

The high-resolution field emission imaging system [12,30] was applied to improve the image resolution of the field emitter distribution on the cathode. In this system, a solenoid (the imaging solenoid in Fig. 4, with the strength denoted as B_i) is used to focus the beam. The focal length depends on the beam energy, which is determined by the emitting phase. Electrons with certain energies (emitting phases) can be selected by placing a collimator with a small aperture after the solenoid. The transverse electron distribution on the last YAG screen of the beam line (denoted as YAG$_3$) can be used to reproduce the field emitter distribution on the cathode with a certain magnification and rotation. The ASTRA simulation study illustrated in Fig. 11 demonstrates the working principle of the imaging system.

The resolution of the system determines the capability of distinguishing emitters on the cathode. Because of the axial
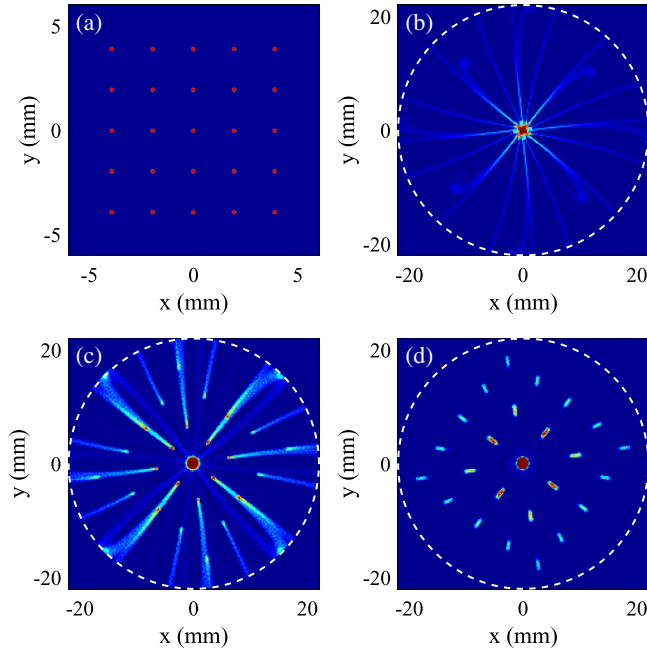
FIG. 11.   ASTRA simulation results of the *in situ* field emission imaging system. (a) Field emitter distribution on the cathode, which consists of 25 ∅0.2 mm emitters separated by 1.77 mm. (b) Electron transverse distribution at the collimator position. (c) Electron transverse distribution on YAG$_3$ without applying the collimator. (d) Electron transverse distribution on YAG$_3$ with a ∅1 mm collimator. In (b)–(d), the white dashed circles represent the ∅44 mm YAG boundary.

symmetry of the imaging system, the resolution can be defined in the radial and angular directions (denoted as R_ρ and R_φ, respectively). Assuming electrons of a zero-size emitter, after collimation they follow Gaussian distributions in both the radial and angular directions with standard deviations of δ_ρ and δ_φ. The resolutions of the imaging system can be expressed as [12,30]

$$R_\rho = 2.35 \times \frac{\delta_\rho}{\overline{\text{mag}}},$$
$$R_\varphi = 2.35 \times \delta_\varphi \rho_0, \tag{5}$$

where $\overline{\text{mag}}$ is the average magnification and ρ_0 is the emitter radial position on the cathode.

Under the experimental conditions ($E_{c,\text{max}}$ of 36 MV/m, B_f of 750 G, B_i of 250 G, and the aperture diameter of 1 mm), R_ρ, R_φ, and $\overline{\text{mag}}$ are simulated to be ∼300 μm, ∼10 μm, and 3.7, respectively. It should be noted that the resolution is not adequate to resolve the fine structure of (N)UNCD emitters whose sizes were determined to be on the order of microns and below in previous dc studies [18,27,28]. The achievable resolution in the experiment could be worse than in the simulation due to the camera resolution, the low signal-to-noise ratio images, the rf amplitude jitter, the variation of E_c within the rf pulse, etc.
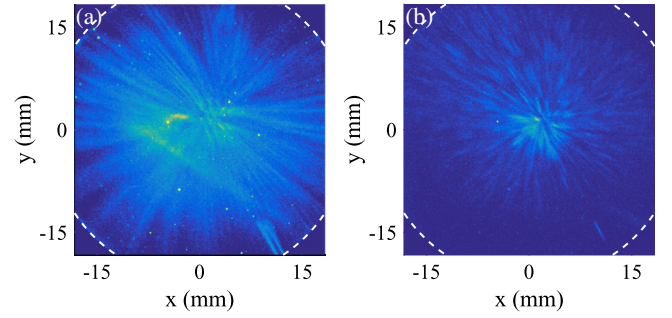

FIG. 12.   Field emission images obtained on YAG$_3$ without a collimator (a) and with a ∅1 mm aperture (b). The white dashed circles represent the ∅44 mm YAG boundary.

As shown in the experiment, however, the *in situ* imaging system is valuable for distinguishing isolated emitters on the cathode.

Field emission images on YAG$_3$ were taken with the high-resolution *in situ* field emission imaging system when the cathode field was conditioned to 36 MV/m, as illustrated in Fig. 12. Each short line-shaped pattern after applying the collimator is caused by a single emitter as suggested in the ASTRA simulation. The observation clearly shows that the field emission current was not uniform from the entire (N)UNCD cathode but had contributions from a large number of isolated emitters. Given the imaging magnification of 3.7 and YAG diameter of 44 mm, the field of view on the cathode that can be observed on YAG$_3$ is ∼∅11.9 mm. Over 100 emitters can be found within this range by counting the short lines, which corresponds to an emitter density above 100/cm^2. The isolated emitter behavior and the emitter density agree with previous observations in dc setups [18,27,28].

C. rf conditioning

The field emission properties of (N)UNCD were studied during rf conditioning by gradually increasing the gun field, $E_{c,\text{max}}$, from ∼8 to ∼42 MV/m. The increment of $E_{c,\text{max}}$ was ∼0.5 MV/m in the conditioning process. The breakdown rate could be as high as 1×10^{-1} per pulse immediately after the increment. $E_{c,\text{max}}$ was not raised until the breakdown rate decreased to 1×10^{-3} per pulse. When a continuous breakdown occurred, the field was reduced to a much lower level until the breakdown stopped, and then the field was pushed back to the breakdown threshold. The entire rf conditioning and measurement process lasted for 40 h.

When conditioned to certain $E_{c,\text{max}}$ levels, e.g., 20 MV/m, 40 MV/m, etc., $E_{c,\text{max}}$ was maintained until the rf breakdown rate dropped below 5×10^{-4} per pulse. Then $E_{c,\text{max}}$ was gradually decreased and B_f was adjusted at each $E_{c,\text{max}}$ to maximize the captured current. According to the aforementioned simulation analysis, the maximum
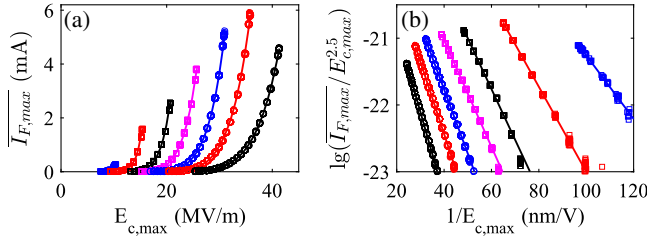
FIG. 13. The dependence of $\overline{I_{F,\max}}$ on $E_{c,\max}$ during rf conditioning, plotted in the $E_{c,\max} - \overline{I_{F,\max}}$ coordinate (a) and the F-N coordinate (b). The dots denote the experimental data, and the lines represent the linear fitting results from the F-N coordinate. The seven curves, from left to right in (a) and from right to left in (b), were taken when $E_{c,\max}$ reached 10, 15, 21, 26, 31, 36, and 42 MV/m, respectively.

capture ratio remains nearly unchanged with $E_{c,\max}$, which ensures accuracy when fitting for β and A_e. The dependence of $\overline{I_{F,\max}}$ on $E_{c,\max}$ is illustrated in Fig. 13. The good linearity in the F-N coordinate suggests that the emission was not space-charge limited [41,42]. It can be seen that $\overline{I_{F,\max}}$ at a fixed field level kept decreasing during rf conditioning. Meanwhile, the maximum achievable $\overline{I_{F,\max}}$ first rose during the conditioning process, reaching ~ 6 mA at $E_{c,\max} = 36$ MV/m and then dropping to ~ 5 mA at $E_{c,\max} = 42$ MV/m.

β and A_e were obtained from fits of the experimental results using Eq. (4) and assuming $\phi = 4.0$ eV. The
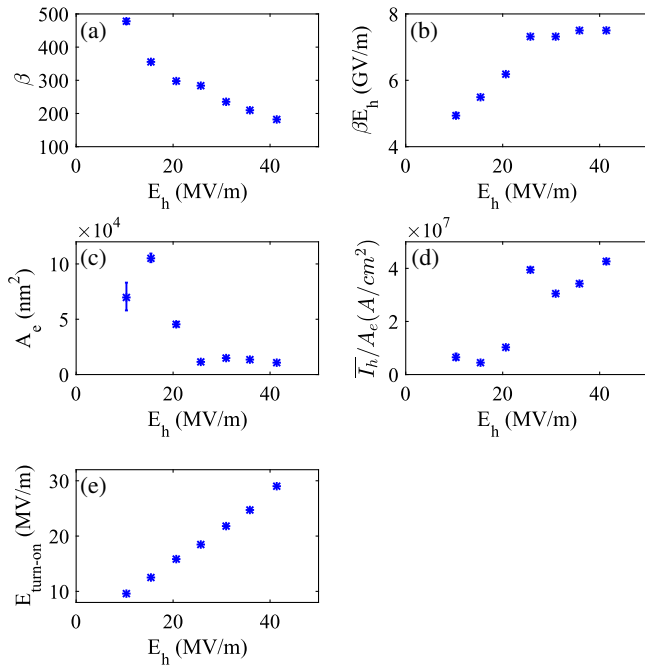

FIG. 14. Evolution of field emission properties during rf conditioning. (a) The field enhancement factor. (b) The maximum microscopic electric field. (c) The effective emission area. (d) The current density. (e) The turn-on field.
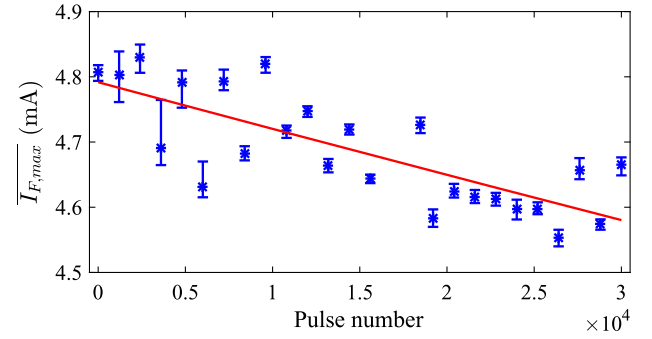

FIG. 15. The current evolution during the 4-h longevity measurement. Blue dots: Measurement results; red line: fitting to $I(t) = I_0 \exp(-t/\tau_l)$.

microscopic field level, the current density, and the turn-on field were derived accordingly, as illustrated in Fig. 14. The turn-on field $E_{\text{turn-on}}$ is defined as the macroscopic field when $\overline{I_{F,\max}}$ reaches 0.1 mA. In Fig. 14, E_h and $\overline{I_h}$ denote the highest achieved $E_{c,\max}$ and the corresponding $\overline{I_{F,\max}}$, respectively. The β value kept decreasing while the turn-on field kept increasing during the rf conditioning, while the maximum microscopic field level βE_h first increased and then reached a stable level of ~ 7.5 GV/m. This value agrees with the one in a previous study where E_h reached ~ 70 MV/m [8]. The A_e value decreased by one order of magnitude to 1×10^4 nm^2, and the current density reached $\sim 4 \times 10^7$ A/cm^2. The behavior of β and the turn-on field are analyzed in the discussion section.

D. Longevity

The longevity of the (N)UNCD cathode was tested when $E_{c,\max}$ reached 42 MV/m. In the 4-h measurement, $\sim 3 \times 10^4$ rf pulses or $\sim 1 \times 10^8$ rf cycles were accumulated and the current dropped by only $\sim 4\%$, as illustrated in Fig. 15. The number of rf pulses was based on the 2.5 μs square emission pulse and 1.3 GHz frequency. The current is assumed to follow $I(t) = I_0 \exp(-t/\tau_l)$, where τ_l denotes the lifetime of the cathode after which the current will be
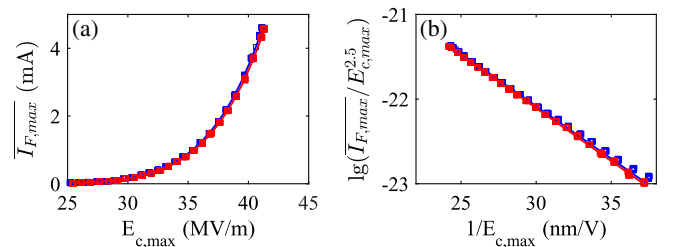

FIG. 16. The dependence of $\overline{I_{F,\max}}$ on $E_{c,\max}$ before (blue) and after (red) the longevity measurement, plotted in the $E_{c,\max} - \overline{I_{F,\max}}$ coordinate (a) and the F-N coordinate (b). The dots denote the experimental data, and the lines represent the linear fitting results from the F-N coordinate.

37% of its initial value. From the 4-h measurement data, τ_l can be fitted to be ~92 h.

Only one breakdown occurred during the measurement. The good longevity and low rf breakdown rate (3×10^{-5} per pulse) demonstrate the promising potential of (N) UNCD material in rf injector applications.

The field emission properties were determined before and after the 4-h longevity measurement, and the difference was negligible, as illustrated in Fig. 16. Together with the significant variation during rf conditioning, it suggests that the evolution of the field emission properties was mainly caused by rf breakdowns rather than accumulated rf pulses.

V. DISCUSSION

In this section, the band diagram of the (N)UNCD material is used to interpret the experimental phenomena observed in this study. These include the nonuniform graphite-to-diamond content distribution revealed by the Raman spectra measurement, nonuniform field emitter distribution revealed by the *in situ* imaging system, the threefold decrease of β and threefold increase of $E_{\text{turn-on}}$ revealed during rf conditioning, and the different behaviors of the surface during the conditioning process when there were remarkable changes of emission properties compared to the longevity measurement when the emission properties remained nearly unchanged.

The basic band diagram of (N)UNCD, viz. the density of states as a function of the energy is illustrated in Fig. 17(a).
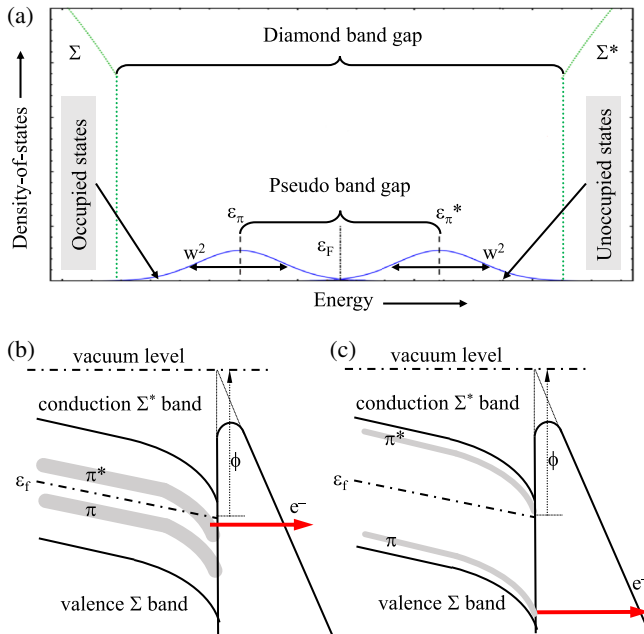

FIG. 17. (a) Density-of-states diagram of (N)UNCD. Surface barrier under the same external macroscopic electric field for sp^2-rich sites (b) and sp^2-poor sites (c). The complete self-consistently solved theory based on Stratton-Baskin-Lvov-Fursey formalism can be found in Ref. [26].

It is modeled as a combination of sp^2 (i.e., graphitic grain boundary) induced π bands inserted into the fundamental band gap of diamond (i.e., host matrix of diamond grains which are sp^3-bonded carbon). The states in the $\pi - \pi^*$ bands can be approximated by Gaussian functions centered at ε_π and ε_{π^*} with variance w^2. It is assumed that $\pi - \pi^*$ and $\Sigma - \Sigma^*$ bands are mirrored with respect to the Fermi level that is pinned inside the pseudo band gap formed by the $\pi - \pi^*$ states. In synthesis, the addition of nitrogen to UNCD always adds a more graphitic phase [47,48], more states in the $\pi - \pi^*$ bands with an increased intensity and width, and a smaller distance between ε_π and ε_{π^*}. The general trend to expect then is that the overlap between $\pi - \pi^*$ bands increases. Consequently, the pseudo band gap becomes smaller (optically darker films [47]) which yields highly conductive semimetallic (N)UNCD.

(N)UNCD is compositionally nonuniform (as illustrated in Fig. 3), and two extreme cases are considered for simplicity: sp^2-rich (N)UNCD sites in Fig. 17(b) and sp^2-poor (N)UNCD sites in Fig. 17(c). The partial penetration of the electric field into the material leads to band bending near the surface. In sp^2-rich (N)UNCD, the π^* band can be therefore lower than the Fermi level in the near-surface layer. Given the strong overlap (enhanced charge exchange) between $\pi - \pi^*$ bands, a large number of electrons are expected to collect near the surface (*metallizing* it). These electrons tunnel through the surface barrier with a larger probability, as they have higher energy positions inside the material as compared to the states normally occupied without an external field perturbation. The result is a high charge carrier concentration and metalliclike behavior which further leads to a high field enhancement factor and low turn-on field [26]. In sp^2-poor (N)UNCD, on the other hand, electrons could come only from the π (or Σ) band with a lower probability of tunneling through the thicker surface barrier. The result is a low field enhancement factor and high turn-on field [26]. Under the same macroscopic field, the current density of sp^2-rich (N) UNCD should be higher than that of sp^2-poor (N)UNCD. This speculation is consistent with the nonuniform emitter distribution revealed by the *in situ* field emission images.

Therefore, the mechanism of (N)UNCD field emission during rf conditioning can be interpreted as follows. (i) Starting at a low surface field, the emission current is dominated by sp^2-rich (N)UNCD sites which causes the high β and low $E_{\text{turn-on}}$ observed in the measurement. (ii) When the surface field is increased during the conditioning progress, a high localized emission current leads to thermally driven degradation and extinction of originally strong emitters [49] which may be presented as rf breakdowns. (iii) At higher fields, sp^2-poor (N)UNCD sites dominate the emission as sp^2-rich locations on the (N)UNCD surface are consumed as conditioning proceeds, leading to low β and high $E_{\text{turn-on}}$. This speculation is consistent with the monotonically decreasing β and the

increasing $E_{\text{turn-on}}$ observed in the experiment. It is also supported by the observation of dramatic emission property changes during the conditioning process with a large number of rf breakdowns versus nearly unchanged emission properties in the longevity measurement with only one rf breakdown detected.

It should be noted that, in the context of the obtained results and the proposed emission mechanism, the near-surface region always has a certain amount of accumulated charge that makes the charge-field relation Fowler-Nordheim-like, with no observable saturation effects [26] due to the low duty cycle of the ACT beam line. Therefore, the application of the classical Fowler-Nordheim law is possible: It simplifies the analysis and makes the comparison between different geometries and material modifications reasonably good. Strictly speaking, the Stratton-Baskin-Lvov-Fursey formalism should be considered for semiconductor and semimetal material analysis and modeling: This is, however, an exceptionally complex problem that is out of the scope of the presented study.

VI. SUMMARY AND FUTURE STUDIES

This study systematically benchmarked the field emission properties of a planar nitrogen-incorporated ultrananocrystalline diamond during the rf conditioning process where the macroscopic field was pushed from ~ 8 to ~ 42 MV/m. The cathode reached a maximum charge of 15 nC and an average emission current of 6 mA during a 2.5 μs emission period. The charge dropped by only $\sim 4\%$ during a 4-h longevity measurement at 42 MV/m which accumulated $\sim 3 \times 10^4$ rf pulses or $\sim 1 \times 10^8$ rf cycles. The high-resolution field emission images revealed a large number of field emitters on the cathode with a density over $100/\text{cm}^2$. This study demonstrates the good potential of (N)UNCD cathodes for application in FEC-based injectors. The observed conditioning effects can all be reasonably explained using the band structure of the material, which, in turn, provides insights for guiding further material engineering with the goal of improved cathode performance.

Future work includes experiments to study the emittance of (N)UNCD field emission cathodes, a comparison between the trend of the emission area calculated by the F-N equation and that of sp^2-rich and sp^2-poor sites directly observed by high-resolution Raman mapping, and the design of electron sources based on the parameter space reported in this manuscript.

[1] C. A. Brau, High-brightness electron beams-small free-electron lasers, Nucl. Instrum. Methods Phys. Res., Sect. A **407**, 1 (1998).

[2] G. N. Fursey, *Field Emission in Vacuum Microelectronics* (Springer Science, New York, 2007).

[3] S. Leemann, A. Streun, and A. Wrulich, Beam characterization for the field-emitter-array cathode-based low-emittance gun, Phys. Rev. Accel. Beams **10**, 071302 (2007).

[4] J. Lewellen and J. Noonan, Field-emission cathode gating for rf electron guns, Phys. Rev. Accel. Beams **8**, 033502 (2005).

[5] R. Ganter, R. Bakker, C. Gough, M. Paraliev, M. Pedrozzi, F. Le Pimpec, L. Rivkin, and A. Wrulich, Nanosecond field emitted and photo-field emitted current pulses from ZrC tips, Nucl. Instrum. Methods Phys. Res., Sect. A **565**, 423 (2006).

[6] X. Li, M. Li, L. Dan, Y. Liu, and C. Tang, Cold cathode rf guns based study on field emission, Phys. Rev. Accel. Beams **16**, 123401 (2013).

[7] P. Piot, C. Brau, B. Choi, B. Blomberg, W. Gabella, B. Ivanov, J. Jarvis, M. Mendenhall, D. Mihalcea, H. Panuganti *et al.*, Operation of an ungated diamond field-emission array cathode in a L-band radiofrequency electron source, Appl. Phys. Lett. **104**, 263504 (2014).

[8] S. V. Baryshev, S. Antipov, J. Shao, C. Jing, K. J. Pérez Quintero, J. Qiu, W. Liu, W. Gai, A. D. Kanareykin, and A. V. Sumant, Planar ultrananocrystalline diamond field emitter in accelerator radio frequency electron injector: Performance metrics, Appl. Phys. Lett. **105**, 203505 (2014).

[9] D. Mihalcea, L. Faillace, J. Hartzell, H. Panuganti, S. Boucher, A. Murokh, P. Piot, and J. Thangaraj, Measurement of Ampère-class pulsed electron beams via field emission from carbon-nanotube cathodes in a radiofrequency gun, Appl. Phys. Lett. **107**, 033502 (2015).

[10] J. Qiu, S. S. Baturin, K. K. Kovi, O. Chubenko, G. Chen, R. Konecny, S. Antipov, A. V. Sumant, C. Jing, and S. V. Baryshev, Nanodiamond thin film field emitter cartridge for miniature high-gradient radio frequency X -band electron injector, IEEE Trans. Electron Devices **65**, 1132 (2018).

[11] X. Li, M. Li, L. Dan, T. He, Y. Liu, Z. Xu, and C. Tang, A double-frequency rf gun for field emission, Nucl. Instrum. Methods Phys. Res., Sect. A **783**, 1 (2015).

[12] J. Shao, J. Shi, S. P. Antipov, S. V. Baryshev, H. Chen, M. Conde, W. Gai, G. Ha, C. Jing, F. Wang *et al.*, In Situ Observation of Dark Current Emission in a High Gradient rf Photocathode Gun, Phys. Rev. Lett. **117**, 084801 (2016).

[13] K. B. Teo, E. Minoux, L. Hudanski, F. Peauger, J.-P. Schnell, L. Gangloff, P. Legagneux, D. Dieumegard, G. A. Amaratunga, and W. I. Milne, Carbon nanotubes as cold cathodes, Nature (London) **437,** 968 (2005).

[14] Q. Wang, X. Li, Y. Di, C. Yu, X. Zhang, M. Li, and W. Lei, High brightness field emission from printed carbon nanotubes in an S-band microwave gun, J. Appl. Phys. **119,** 084504 (2016).

[15] D. Zhou, A. Krauss, L. Qin, T. McCauley, D. Gruen, T. Corrigan, R. P. Chang, and H. Gnaser, Synthesis and electron field emission of nanocrystalline diamond thin films grown from N_2/CH_4 microwave plasmas, J. Appl. Phys. **82,** 4546 (1997).

[16] T. Ikeda and K. Teii, Origin of low threshold field emission from nitrogen-incorporated nanocrystalline diamond films, Appl. Phys. Lett. **94,** 143102 (2009).

[17] R. J. Nemanich, J. A. Carlisle, A. Hirata, and K. Haenen, CVD diamond-Research, applications, and challenges, MRS Bull. **39,** 490 (2014).

[18] O. Chubenko, S. S. Baturin, K. K. Kovi, A. V. Sumant, and S. V. Baryshev, Locally resolved electron emission area and unified view of field emission from ultrananocrystalline diamond films, ACS Appl. Mater. Interfaces **9,** 33229 (2017).

[19] N. Shang, P. Papakonstantinou, P. Wang, A. Zakharov, U. Palnitkar, I.-N. Lin, M. Chu, and A. Stamboulis, Self-assembled growth, microstructure, and field-emission high-performance of ultrathin diamond nanorods, ACS Nano **3,** 1032 (2009).

[20] V. Krivchenko, A. Pilevsky, A. Rakhimov, B. Seleznev, N. Suetin, M. Timofeyev, A. Bespalov, and O. Golikova, Nanocrystalline graphite: Promising material for high current field emission cathodes, J. Appl. Phys. **107,** 014315 (2010).

[21] K. Teii and M. Nakashima, Synthesis and field emission properties of nanocrystalline diamond/carbon nanowall composite films, Appl. Phys. Lett. **96,** 023112 (2010).

[22] I. Levchenko, S. Xu, G. Teel, D. Mariotti, M. Walker, and M. Keidar, Recent progress and perspectives of space electric propulsion systems based on smart nanomaterials, Nat. Commun. **9,** 879 (2018).

[23] V. Chatterjee, R. Harniman, P. W. May, and P. Barhai, Direct observation of electron emission from the grain boundaries of chemical vapour deposition diamond films by tunneling atomic force microscopy, Appl. Phys. Lett. **104,** 171907 (2014).

[24] R. L. Harniman, O. J. Fox, W. Janssen, S. Drijkoningen, K. Haenen, and P. W. May, Direct observation of electron emission from grain boundaries in CVD diamond by PeakForce-controlled tunnelling atomic force microscopy, Carbon **94,** 386 (2015).

[25] E. Wang at Brookhaven National Laboratory (private communication).

[26] O. Chubenko, S. S. Baturin, and S. V. Baryshev, Theoretical evaluation of electronic density-of-states and transport effects on field emission from n-type ultrananocrystalline diamond films, J. Appl. Phys. **125,** 205303 (2019).

[27] J. Cui and J. Robertson, Field emission from chemical vapor deposition diamond surface with graphitic patches, J. Vac. Sci. Technol. B **20,** 238 (2002).

[28] F. Köck, J. Garguilo, and R. Nemanich, Direct correlation of surface morphology with electron emission sites for intrinsic nanocrystalline diamond films, Diam. Relat. Mater. **13,** 1022 (2004).

[29] J. Shao, S. P. Antipov, S. V. Baryshev, H. Chen, M. Conde, D. S. Doran, W. Gai, C. Jing, W. Liu, J. Power et al., Observation of Field-Emission Dependence on Stored Energy, Phys. Rev. Lett. **115,** 264802 (2015).

[30] J. Shao, *Investigations on rf Breakdown Phenomenon in High Gradient Accelerating Structures* (Springer, New York, 2018).

[31] D. Xiang, W.-H. Huang, Y.-C. Du, L.-X. Yan, R.-K. Li, C.-X. Tang, Y.-Z. Lin, S.-J. Park, and J. Park, in *Proceedings of the 22nd Particle Accelerator Conference, PAC-2007, Albuquerque, NM* (IEEE, New York, 2007), pp. 1049–1051.

[32] H. J. Qian, C. Li, Y. C. Du, L. X. Yan, J. F. Hua, W. H. Huang, and C. X. Tang, Experimental investigation of thermal emittance components of copper photocathode, Phys. Rev. Accel. Beams **15,** 040102 (2012).

[33] T. Corrigan, D. Gruen, A. Krauss, P. Zapol, and R. P. Chang, The effect of nitrogen addition to Ar/CH_4 plasmas on the growth, morphology and field emission of ultra-nanocrystalline diamond, Diam. Relat. Mater. **11,** 43 (2002).

[34] T. Nikhar, R. Rechenberg, M. Becker, and S. V. Baryshev, Revisiting Effects of Nitrogen Incorporation and Graphitization on Conductivity of Ultra-nano-crystalline Diamond Films, arXiv:1910.09595.

[35] K. J. Pérez Quintero, S. Antipov, A. V. Sumant, C. Jing, and S. V. Baryshev, High quantum efficiency ultrananocrystalline diamond photocathode for photoinjector applications, Appl. Phys. Lett. **105,** 123103 (2014).

[36] G. Chen, G. Adhikari, L. Spentzouris, K. K. Kovi, S. Antipov, C. Jing, W. Andreas Schroeder, and S. V. Baryshev, Mean transverse energy of ultrananocrystalline diamond photocathode, Appl. Phys. Lett. **114,** 093103 (2019).

[37] J. Wang and G. Loew, Field emission and rf breakdown in high-gradient room-temperature linac structures, Stanford Linear Accelerator Center, Technical Report No. SLAC-PUB-7684, 1997.

[38] R. H. Fowler and L. Nordheim, Electron emission in intense electric fields, Proc. R. Soc. A **119,** 173 (1928).

[39] R. Huang, D. Filippetto, C. Papadopoulos, H. Qian, F. Sannibale, and M. Zolotorev, Dark current studies on a normal-conducting high-brightness very-high-frequency electron gun operating in continuous wave mode, Phys. Rev. Accel. Beams **18,** 013401 (2015).

[40] K. Flöttmann, ASTRA-A space charge tracking algorithm, DESY.

[41] J. Barbour, W. Dolan, J. Trolan, E. Martin, and W. Dyke, Space-charge effects in field emission, Phys. Rev. **92,** 45 (1953).

[42] A. Rokhlenko, K. L. Jensen, and J. L. Lebowitz, Space charge effects in field emission: One dimensional theory, J. Appl. Phys. **107,** 014904 (2010).

[43] J. Han, J. Bähr, H. Grabosch, M. Krasilnikov, V. Miltchev, A. Oppelt, and B. Petrosyan, in *Proceedings of the 21st*

Particle Accelerator Conference, Knoxville, TN, 2005 (IEEE, Piscataway, NJ, 2005), pp. 895–897.

[44] A. Moretti, Z. Qian, J. Norem, Y. Torun, D. Li, and M. Zisman, Effects of high solenoidal magnetic fields on rf accelerating cavities, Phys. Rev. Accel. Beams **8**, 072001 (2005).

[45] D. Dowell, E. Jongewaard, C. Limborg-Deprey, J. Schmerge, and A. Vlieks, in *Proceedings of the 22nd Particle Accelerator Conference, PAC-2007, Albuquerque, NM* (IEEE, New York, 2007), pp. 1299–1301.

[46] R. Xiang, A. Arnold, T. Kamps, P. Lu, P. Michel, P. Murcek, H. Vennekate, G. Staats, and J. Teichert, Experimental studies of dark current in a superconducting rf photoinjector, Phys. Rev. ST Accel. Beams **17**, 043401 (2014).

[47] M. Nesládek, K. Meykens, L. Stals, M. Vaněček, and J. Rosa, Origin of characteristic subgap optical absorption in CVD diamond films, Phys. Rev. B **54**, 5552 (1996).

[48] P. Zapol, M. Sternberg, L. A. Curtiss, T. Frauenheim, and D. M. Gruen, Tight-binding molecular-dynamics simulation of impurities in ultrananocrystalline diamond grain boundaries, Phys. Rev. B **65**, 045403 (2001).

[49] S. S. Baturin, T. Nikhar, and S. V. Baryshev, Field electron emission induced glow discharge in a nanodiamond vacuum diode, J. Phys. D **52**, 325301 (2019).